The Astrophysical Journal, 997:313 (10pp), 2026 February 1 https://doi.org/10.3847/1538-4357/ae2de6

Energetic Nonthermal Electrons within the Above-the-looptop Regions in Solar Flares: Acceleration, Feedback, and Quasiperiodic Pulsations

Jeongbhin Seo[1], Fan Guo[1,2], Xiaocan Li[1], Bin Chen[3], Chengcai Shen[4], and Hui Li[1]
[1] Los Alamos National Laboratory, Los Alamos, NM 87545, USA
[2] New Mexico Consortium, Los Alamos, NM 87544, USA
[3] Center for Solar-Terrestrial Research, New Jersey Institute of Technology, 323 Dr. Martin Luther King Jr. Boulevard, Newark, NJ 07102-1982, USA
[4] Harvard-Smithsonian Center for Astrophysics, 60 Garden Street, Cambridge, MA 02138, USA
Received 2025 May 13; revised 2025 December 10; accepted 2025 December 14; published 2026 January 29

Abstract

Solar flares are among the most dramatic events in the solar system, releasing substantial magnetic energy and accelerating a large number of electrons to high energies. Notably, in certain events, the above-the-looptop region may contain a significant population of nonthermal electrons, both in number and energy. For the first time, we adopt a novel numerical method that combines magnetohydrodynamics with energetic particles incorporating feedback from nonthermal electrons to investigate electron acceleration and transport in solar flares. We find that a large fraction of energetic electrons are accelerated via the current sheet and termination shock regions. Most energetic electrons are concentrated in the above-the-looptop region, carrying a sizable amount of the released energy. We observe that greater feedback of nonthermal electrons leads to steeper energy spectra. The energy density of the nonthermal electrons oscillates due to the periodic impact of magnetic islands into the above-the-looptop region, which may help explain the observed quasiperiodic pulsations. Our simulations provide new insights into the origin of nonthermal electrons and associated emissions in the above-the-looptop region.

Unified Astronomy Thesaurus concepts: Solar flares (1496)

1. Introduction

During solar flares, magnetic reconnection drives rapid release of a substantial amount of magnetic energy (H. Carmichael 1964; P. A. Sturrock 1966; T. Hirayama 1974; R. A. Kopp & G. W. Pneuman 1976), resulting in strong plasma heating and nonthermal particle acceleration. A significant portion of the released energy is believed to be carried by nonthermal electrons (e.g., S. Krucker et al. 2010; M. Oka et al. 2013, 2015; A. Warmuth & G. Mann 2020), and understanding the mechanisms behind their acceleration remains a central focus of solar flare research.

The multiwavelength emissions (hard X-rays and microwaves) generated by these accelerated electrons provide valuable insights into particle acceleration, transport, and radiation processes. These observations have revealed that nonthermal electrons typically exhibit a power-law energy spectrum, $f(\varepsilon) \quad \varepsilon^{-}$, with a median spectral index of 5 (S. Krucker et al. 2010; M. Oka et al. 2013, 2015; F. Effenberger et al. 2017). Hard X-ray observations suggest that, in certain events, a significant fraction of electrons are accelerated into the nonthermal range, carrying energy comparable to the released magnetic energy (S. Krucker et al. 2010; M. Oka et al. 2013, 2015). Especially, recent EOVSA observations along with other multiwavelength observations have provided unprecedented imaging spectroscopy of the X8.2-class eruptive flare event SOL2017-09-10 (D. E. Gary et al. 2018; B. Chen et al. 2020b; G. D. Fleishman et al. 2022). These observations show that the nonthermal electrons are partially confined to the above-the-looptop region with a relatively weak magnetic strength, referred to as the "magnetic bottle" (X. Kong et al. 2019; B. Chen et al. 2020b, 2024). It has been suggested that the above-the-looptop region is the primary region for energetic particle acceleration and trapping in this event, although further studies are needed to see if this is a universal scenario.

G. D. Fleishman et al. (2022) also presented spatially resolved distributions of thermal and nonthermal electrons in the SOL2017-09-10 flare, based on the analysis of EOVSA data. These distributions suggested that the above-the-looptop region is predominantly filled with nonthermal electrons almost devoid of thermal plasma. It is worth noting that E. P. Kontar et al. (2023) studied the same flare and concluded that the fraction of nonthermal electrons in the above-the-looptop region was much lower than that estimated by G. D. Fleishman et al. (2022). Nevertheless, numerous studies have suggested that a large fraction of the accelerated electrons in the flare region are nonthermal (S. Krucker et al. 2010; M. Oka et al. 2013, 2015; G. D. Fleishman et al. 2022). These suggest that feedback from nonthermal electrons may play an important role in the above-the-looptop region.

Studying such efficient electron acceleration in solar flares requires new methods to capture the acceleration processes, the large-scale flare dynamics, and the potential feedback from energetic electrons to the background plasmas. Recently, we developed a novel method for simulating particle acceleration with feedback from energetic particles, called the magnetohydrodynamics-stochastic differential equation (MHD-SDE) method (J. Seo et al. 2024). This method incorporates feedback from the pressure of nonthermal particles in MHD simulations, obtained by solving Parker's transport equation (E. N. Parker 1965) using the SDE method. The Parker transport equation includes the spatial diffusion of nonthermal particles by MHD turbulence, allowing for more realistic simulation of transport and acceleration.

For the first time, we apply the MHD-SDE method to a flare eruption geometry, focusing on the above-the-looptop region where nonthermal electron numbers and energies are prominent. By investigating nonthermal electron distributions

and acceleration mechanisms in this region, we aim to enhance our understanding of solar flare dynamics and the impact of energetic particle feedback. Our results suggest that nonthermal electrons, accelerated along the current sheet and at the termination shock, follow a power-law energy spectrum whose slope varies depending on the feedback of the nonthermal electron. The impact of magnetic islands into the above-the-looptop region generates oscillations in the energy density of nonthermal electrons, which may lead to the generation of quasiperiodic pulsations (QPPs). The paper is organized as follows: Section 2 introduces the numerical method, followed by a discussion of the simulation results in Section 3. A brief summary and outlook are provided in Section 4.

2. Numerical Method

2.1. MHD-SDE Model

Several approaches have been developed to incorporate the feedback of nonthermal components at the hydrodynamic scale (see M. Ruszkowski & C. Pfrommer 2023 for a review). A common approach is to include feedback effects of energetic particles in the MHD equations. Examples include the *kglobal* model (J. F. Drake et al. 2019; H. Arnold et al. 2021), the MHD particle-in-cell (PIC) method (X.-N. Bai et al. 2015; X. Sun & X.-N. Bai 2023), the nonlinear kinetic Monte Carlo model (A. M. Bykov et al. 2014, 2024), and the turbulence transport equation coupled with the MHD equation (B.-B. Wang et al. 2022). However, none of these methods have been applied to solar flares with a realistic magnetic geometry.

For the first time, we have taken into account the feedback from nonthermal electrons in an eruptive flare geometry. These electrons are accelerated and carry a significant fraction of the released energy. We have developed the MHD-SDE method to simulate systems where the pressure from nonthermal particles is significant (J. Seo et al. 2024). This method solves the MHD equations with feedback from the nonthermal particles. To implement this feedback, we obtain the nonthermal pressure from the distribution function of the nonthermal component, which is derived from Parker's transport equation using the SDE.

The resistive MHD equations with nonthermal fluid feedback are derived as (J. Seo et al. 2024)

$$\frac{\partial \rho}{\partial t} + \nabla \cdot (\rho \boldsymbol{v}) = -S_\rho, \tag{1}$$

$$\frac{\partial \rho \boldsymbol{v}}{\partial t} + \nabla \cdot (\rho \boldsymbol{v}\boldsymbol{v} + P^* \boldsymbol{I} - \boldsymbol{B}\boldsymbol{B}) = -\nabla \cdot P_{\rm NT} \boldsymbol{I} - S_m, , \tag{2}$$

$$\frac{\partial E}{\partial t} + \nabla \cdot [(E + P^*)\boldsymbol{v} - \boldsymbol{B}(\boldsymbol{B} \cdot \boldsymbol{v})] = \nabla \cdot (\boldsymbol{B} \times \eta \boldsymbol{j}) - \boldsymbol{v} \cdot (\nabla \cdot P_{\rm NT} \boldsymbol{I}) - S_E, \tag{3}$$

$$\frac{\partial \boldsymbol{B}}{\partial t} - \nabla \times (\boldsymbol{v} \times \boldsymbol{B}) = \eta \nabla^2 \boldsymbol{B}, \tag{4}$$

where

$$E = P_g/(\gamma_g - 1) + (\rho \boldsymbol{v} \cdot \boldsymbol{v} + \boldsymbol{B} \cdot \boldsymbol{B})/2. \tag{5}$$

Here, ρ, $\boldsymbol{v}$, $\boldsymbol{B}$, P_g, $P_{\rm NT}$, $\boldsymbol{j}$, γ_g, and η denote the thermal plasma density, velocity, magnetic field, thermal plasma pressure, nonthermal electron pressure, current density, adiabatic index of the thermal plasma, and resistivity, respectively. P^* is the sum of thermal plasma pressure and magnetic pressure, $P^* = P_g + B^2/2$.

S_ρ, S_m, and S_E are the sink terms due to nonthermal particle injection from thermal plasmas for density, momentum, and energy, respectively, and will be discussed in Section 2.3. In this context, the subscripts g and NT denote the thermal plasma gas and the nonthermal electrons, respectively. Note that our current model omits the effects of thermal conduction, which we defer to a future study. This omission is not unique to our work (e.g., J. T. Dahlin et al. 2025), as incorporating all the multiphysics effects (including energetic particles, the focus of the current study) during solar flares remains very demanding.

We solve Parker's transport equation for nonthermal electrons to obtain their distribution as follows:

$$\frac{\partial f}{\partial t} + (\boldsymbol{v} + \boldsymbol{v_d}) \cdot \nabla f - \frac{1}{3} \nabla \cdot \boldsymbol{v} \frac{\partial f}{\partial \ln p_{\rm NT}} = \nabla \cdot (\boldsymbol{\kappa} \nabla f) + Q, \tag{6}$$

where $f(x_{\rm NT}, p_{\rm NT}, t)$ is the distribution function, which is a function of position, $x_{\rm NT}$, momentum, $p_{\rm NT}$, and time, t. $\boldsymbol{v_d}$ and $\boldsymbol{\kappa}$ are the particle drift velocity and the spatial diffusion tensor, respectively. In our simulation, we only consider cases where $\boldsymbol{v_d}$ is negligible, which is a good approximation for solar flare reconnection (e.g., $\boldsymbol{v}_d$ 0.02 km s^{-1} for 10 keV electrons, a current sheet thickness of 100 km, and a magnetic field of 100 G (P. A. Isenberg & J. R. Jokipii 1979)). Q is the source term with the injection distribution $s(p_{\rm NT})$, which will be discussed in Section 2.3. We solve this equation using the SDE; the detailed method is described in X. Li et al. (2018b). To incorporate the feedback from nonthermal particles into the MHD equations, we treat the bulk population of nonthermal electrons as a fluid. The pressure from the nonthermal fluid is given by

$$P_{\rm NT} = \frac{1}{3} \int v_{\rm NT}\, p_{\rm NT}\, f\,(x_{\rm NT}, p_{\rm NT}, t)\, d^3 p_{\rm NT}, \tag{7}$$

where the speed of nonthermal particles is

$$v_{\rm NT} = \frac{p_{\rm NT} c^2}{\sqrt{p_{\rm NT}^2 c^2 + m_e^2 c^4}},$$

where m_e and c are the electron mass and the speed of light, respectively. This form is applicable for particles with energies from nonrelativistic to relativistic regimes.

The Parker transport equation assumes a nearly isotropic momentum distribution due to frequent pitch-angle scattering, thereby incorporating the effects of spatial diffusion and compression acceleration of energetic particles. This assumption is well supported by numerical studies. For example, first-principle PIC simulations have shown that compression energization is critical for accelerating high-energy particles in reconnection with a weak guide field, where particle distributions remain nearly isotropic and shear acceleration is inefficient due to low anisotropy (X. Li et al. 2018a). MHD simulations further suggest that reconnection layers are compressible, particularly at low plasma and with weak guide fields (J. Birn et al. 2012; E. Provornikova et al. 2016); in eruptive flare simulations, strong guide fields can weaken

significantly during peak reconnection (J. T. Dahlin et al. 2022), and weak guide field models better match observed magnetic structures in the SOL2017-09-10 flare (B. Chen et al. 2020b).

Earlier studies have also shown that turbulence generated during 3D reconnection can efficiently scatter high-energy particles, leading to nearly isotropic distributions (X. Li et al. 2019a). In addition, energetic electrons can excite plasma waves and associated structures that act to scatter and confine them (e.g., T. C. Li et al. 2013; H. Ma et al. 2023). Observational evidence supports this picture. For instance, B. Chen et al. (2020a) reported footpoint microwave emissions delayed by nearly 20 s compared to flux-rope sources, much longer than the subsecond travel time expected for 100 keV electrons under free streaming. Similarly, S. Mondal et al. (2024) showed that assuming free streaming leads to an order-of-magnitude overestimate of footpoint fluxes. Together, these findings underscore the essential role of scattering in nonthermal electron transport.

In our study, the confinement of energetic electrons is due to spatial diffusion as particles are scattered in the looptop region. It is worth noting that the Parker transport equation does not explicitly include effects with pitch-angle dependence, such as magnetic mirroring. Some studies have investigated electron acceleration in solar flare regions by solving the focused transport equation, which includes pitch-angle dependence and magnetic mirroring, but they yield a similar nonthermal electron distribution compared to that obtained from the Parker equation (X. Kong et al. 2019, 2022). Further studies will be required to better understand the mechanism for confining energetic electrons at the looptop regions.

2.2. Simulation Setup

We carry out 2.5D MHD-SDE simulations of the coronal mass ejection/flare eruption model described by B. Chen et al. (2020b), in which a preexisting magnetic flux rope erupts along with a vertical reconnection current sheet (T. G. Forbes & E. R. Priest 1995; J. Lin & T. G. Forbes 2000). This model initially exhibits an X-point of magnetic reconnection located below the flux rope, where an extending vertical current sheet gradually develops as the flux rope erupts. The upper section of the vertical current sheet originates from the base of the flux rope and narrows as it extends downward, eventually connecting with its lower counterpart above the flare arcade, which broadens at lower heights (see Figure 1).

We start the simulation without a guide field to capture the impulsive phase when the magnetic energy release and particle acceleration are most efficient.

We normalize the simulations by $L_0 = 300$ Mm, $B_0 = 50$ G, and $n_0 = 2.5 \times 10^9\,\mathrm{cm}^{-3}$. These values are within the reported ranges of typical parameters of solar flares: magnetic field strengths of B 10–100 G (H. Lin et al. 2000; Z. Yang et al. 2020; D. H. Brooks et al. 2021) and thermal electron number densities of n_T $10^9\,\mathrm{cm}^{-3}$ (H. P. Warren & D. H. Brooks 2009; P. R. Young et al. 2009; G. Del Zanna et al. 2023). The simulation domain spans $-45 < x < 45$ Mm and $0 < y <$ 180 Mm. The speed is normalized by the characteristic Alfvén speed, $V_{A0} = 2181\,\mathrm{km\,s}^{-1}$, and the corresponding normalized timescale is $\tau_A = L_0/V_{A0}$ 137 s. In our model, the plasma beta in the vertical current sheet has a value of approximately 0.1, corresponding to a current sheet temperature of T_{CS} 10^7 K. We adopt a uniform resistivity $\eta = 10^{-6}$ resulting in a Lundquist number of $S = L_y V_{A0}/\eta = 6 \times 10^5$. Although the typical solar coronal conditions correspond to $S = 10^{12}$–10^{14}, the reconnection rate becomes independent of S for $S \gtrsim 10^4$ (A. Bhattacharjee et al. 2009; N. F. Loureiro & D. A. Uzdensky 2016). Therefore, our case can represent the reconnection rate of a high-Lundquist-number current sheet. The grid numbers are $n_x \times n_y =$ 2048×4096, so the grid resolution is $\Delta x = \Delta y$ 0.04 Mm. The simulation resolves the half-thickness of the current sheet with approximately 10 cells, which is sufficient to capture the magnetic islands that form along the sheet.

We adopt a spatial diffusion coefficient from quasi-linear theory, assuming magnetic turbulence has an isotropic, Kolmogorov-like power spectrum. This is given as (J. Giacalone & J. R. Jokipii 1999)

$$\kappa_{\parallel}(p_{\mathrm{NT}}) = \frac{3\, v_{\mathrm{NT}}^3}{20\, L_c\, \Omega_{\mathrm{NT}}^2\, \sigma^2} \csc\left(\frac{3\pi}{5}\right) \times \left[1 + \frac{72}{7}\left(\frac{\Omega_{\mathrm{NT}}\, L_c}{v_{\mathrm{NT}}}\right)^{5/3}\right], \tag{8}$$

where $L_c = 140$ km is the turbulence correlation length, and $\sigma^2 = \langle \delta B^2 \rangle / B_0^2 = 1$ (Y.-M. Huang & A. Bhattacharjee 2016) is the normalized wave variance of turbulence. The gyrofrequency is given by

$$\Omega_{\mathrm{NT}} = \frac{qB_0}{\gamma_{\mathrm{NT}}\, m_e c}, \tag{9}$$

where q and γ_{NT} are the electron charge and the Lorentz factor of nonthermal electrons, respectively. The normalization of the spatial diffusion coefficient is given by $\kappa_0 = L_0 v_A$ $6.5 \times 10^{18}\,\mathrm{cm}^2\,\mathrm{s}^{-1}$. In this case, $\kappa_{\parallel}$ $6.1 \times 10^{-5} \kappa_0$ for 10 keV electrons. We assume highly anisotropic spatial diffusion, with $\kappa_{\perp} = 0.01 \kappa_{\parallel}$, based on test particle simulations by J. Giacalone & J. R. Jokipii (1999).

2.3. Injection of Nonthermal Electrons

For magnetic reconnection, the initial nonthermal energization can come from Fermi reflection, pickup process, and nonideal electric field, etc. (F. Guo et al. 2024). Not all of them can be included unless fully kinetic simulations can be used. Fully kinetic simulations have shown that a few tens of percent of thermal electrons can be accelerated into a nonthermal distribution in regions where magnetic reconnection occurs, depending on parameters such as the guide field strength (O. French et al. 2023). Based on this result, in this paper, we introduce a straightforward approach: a constant fraction of thermal electrons is injected into the nonthermal population within the magnetic reconnection region, identified by high current density. This injected population represents suprathermal particles that would be produced by kinetic preacceleration mechanisms such as Fermi reflection in low guide field reconnection (e.g., Q. Zhang et al. 2021; O. French et al. 2023; F. Guo et al. 2024). Our model treats the injection fraction, R_i, as a control parameter due to its uncertainty arising from dependence on local plasma conditions, such as the plasma beta and guide field strength.

To set a certain density injection of nonthermal electrons, we first add "seed particles" throughout the entire domain. In this study, we set the total number of these particles to be n_{seed} 10^9. These seed particles are initially massless and do

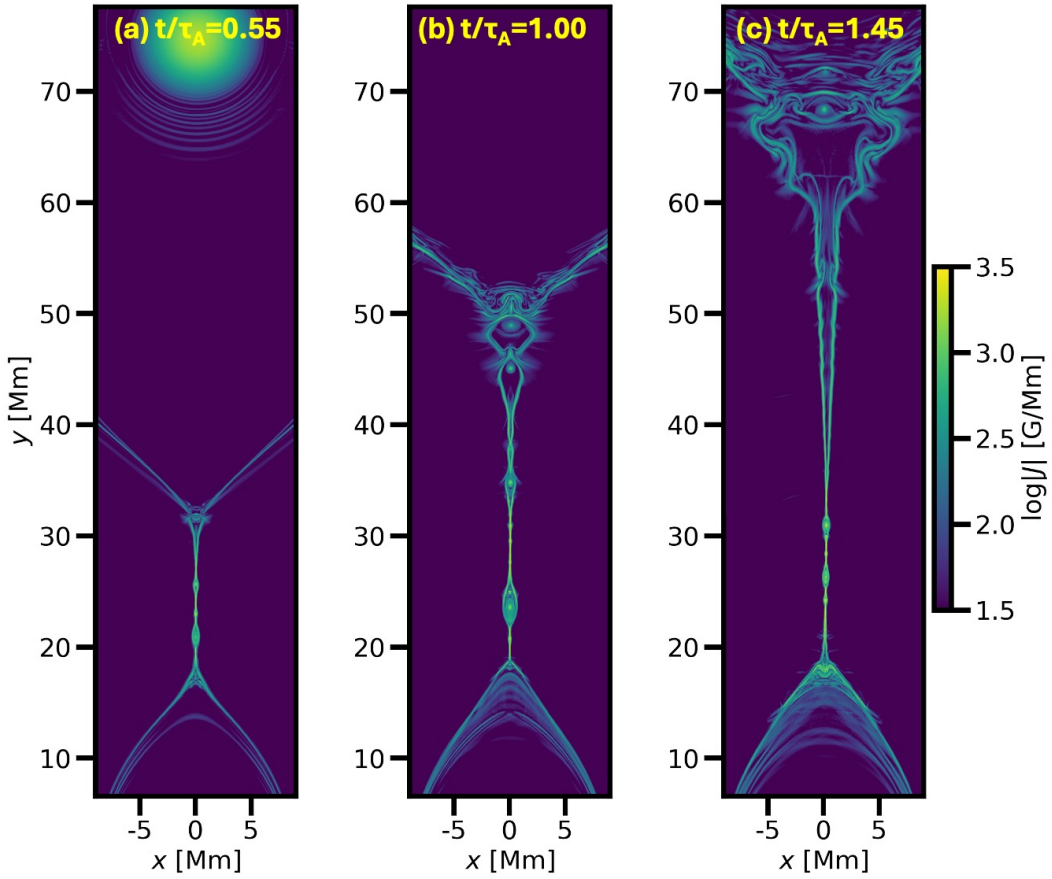

Figure 1. Snapshots of the electric current density $\log|J|$ at (a) $t/\tau_A = 0.55$, (b) 1.0, and (c) 1.45. Only the [-10, 10] × [6, 75]Mm^2 domain is shown here. The eruption of the flux rope induces magnetic reconnection along the vertical current sheet and generates multiple plasmoids. The reconnection layer is distinguished by high current density regions.

not provide any feedback to the MHD fluid. They are simply advected by the background plasma flow. When they are advected into a high current density region, they are tagged as "nonthermal" particles, representing the injection process. In this simulation, the threshold for the high current density region is set to $|J| \geqslant 10^3\,\mathrm{G\,Mm^{-1}}$, but the final result is not very sensitive to the threshold within a range of an order of magnitude. We assign the density of the nonthermal particles proportional to the thermal density to achieve a specific density ratio between nonthermal electrons and the background thermal electron density, $R_i = n_{\rm NT}/n_T$. For the fiducial case, we assume that $R_i = 10\%$ of thermal electrons are preaccelerated to nonthermal energies. We also simulate $R_i = 1\%$ and $R_i = 20\%$ injection cases for comparison.

In PIC simulations, the injection energy of nonthermal electrons, which corresponds to the starting point of the power-law energy spectrum, is approximately $\approx 0.2 m_p v_A^2 \approx 10$ keV (Q. Zhang et al. 2021, 2024), where m_p is the proton mass. Accordingly, we set the injection energy to $\varepsilon_{\rm inj} = 10$ keV.

A particle-splitting scheme is adopted to increase statistics, and we set it up in such a way that the particles' total mass remains conserved. Once tagged as "nonthermal particles," particles follow Parker's transport equation and provide feedback as described by Equations (2) and (3).

When the injection of "nonthermal particle" occurs, a thermal electron is converted into a nonthermal electron. As a result, the plasma density, momentum density, and energy density within each cell are reduced by the amount corresponding to the injected nonthermal particles by adding sink terms,

$$S_\rho = \frac{m_e}{V\Delta t}\int s(p_{\rm NT})\,dp^3_{\rm NT}, \tag{10}$$

$$S_m = \frac{m_e \boldsymbol{v}}{V\Delta t}\int s(p_{\rm NT})\,dp^3_{\rm NT}, \tag{11}$$

$$S_E = \frac{m_e v^2}{2V\Delta t}\int s(p_{\rm NT})\,dp^3_{\rm NT} + \frac{1}{\Delta t}\int E(p_{\rm NT})\,s(p_{\rm NT})\,dp^3_{\rm NT}, \tag{12}$$

on the right side of Equations (1)–(3), where V, Δt, and m_e are the volume of the cell, the step size of the MHD, and the mass of the electron, respectively. s is the distribution function of the injected particles. Here, we use a monoenergy injection $s(p_{\rm NT}) = n_{\rm inj}\ (p_{\rm NT} - p_{\rm inj})$, where $n_{\rm inj}$ denotes the number of nonthermal electrons injected within a cell during the time interval Δt, and $p_{\rm inj}$ represents the momentum of an electron with 10 keV energy. The second term on the right-hand side of S_E represents the energy transfer from the internal energy of the thermal plasma to nonthermal electrons to ensure energy conservation. The integration occurs for all injected nonthermal particles within Δt in each cell.

In our previous study (J. Seo et al. 2024), we assumed a population of preexisting seed particles as "preselected" to allow particle acceleration through the Parker transport equation. A similar approach is also used in the *kglobal* simulations (e.g., H. Arnold et al. 2021). In this paper, instead of assigning "preselected" particles in the coronal background, we mimic the injection process observed in PIC simulations by injecting "preaccelerated" particles at the magnetic reconnection region. We have compared the two models and found quantitatively similar results, which indicate that the choice of initialization of particles is not critical for the final outcome.

3. Simulation Results

3.1. Evolution of the Flare Eruption Model

The large-scale evolution of the flare eruption model includes the formation of the current sheet and the eruption of the flux rope. We find that feedback from nonthermal electrons does not significantly alter the global characteristics of the eruptive flare, such as the flux-rope eruption and magnetic reconnection in the vertical current sheet. While there are some differences in the fine-scale features, such as plasmoid formation and motion, the overall outflow and the morphology of the eruption and looptop remain similar.

The flare eruption model initially shows that the rising flux rope stretches the underlying field lines, forming an elongated current sheet. Reconnection along this vertical current sheet enables the flux rope to successfully erupt from the solar surface (J. Lin & T. G. Forbes 2000). Figure 1 shows the time evolution of the current density in this model. As shown in this figure, due to the high S, the unstable current sheet narrows to a smaller scale, leading to the formation and rapid growth of a series of magnetic islands, some of which merge into larger structures (N. F. Loureiro et al. 2007; A. Bhattacharjee et al. 2009; D. A. Uzdensky et al. 2010; N. F. Loureiro & D. A. Uzdensky 2016). The downflow generated by magnetic reconnection impinges on the looptop and creates a termination shock (C. Shen et al. 2018; X. Kong et al. 2019). These current sheet regions and the termination shock are expected to accelerate particles efficiently.

3.2. Acceleration of Nonthermal Electrons

To identify regions of efficient acceleration during the flare eruption, we track the acceleration rate, $= (\Delta\varepsilon/\varepsilon)/\Delta t$, where ε is the kinetic energy of a nonthermal electron. measures how rapidly particles can be accelerated. In this paper, is calculated by averaging the acceleration rate of each nonthermal particle within each cell. Δt is one MHD time step, approximately $10^{-3}\tau_A$.

The momentum evolution in Ito-type SDEs can be described as (X. Li et al. 2018b)

$$\Delta p_{\rm NT} = -\frac{p_{\rm NT}}{3}(\nabla \cdot \boldsymbol{v})\Delta t. \quad (13)$$

Therefore,

$$\alpha = \frac{\Delta\varepsilon/\varepsilon}{\Delta t} \propto \frac{\Delta p_{\rm NT}/p_{\rm NT}}{\Delta t} \propto -(\nabla \cdot \boldsymbol{v}). \quad (14)$$

Hence, the acceleration efficiency is proportional to the plasma compression. A positive (negative) value of corresponds to plasma compression (divergence) and indicates particle acceleration (deceleration).

In Figure 2, we present the evolution of for the $R_i = 10\%$ case. We confirmed that the current sheets and the termination shock are regions that host strong compression for accelerating these electrons. Along the vertical current sheet, magnetic reconnection-driven structures, such as reconnection exhausts and magnetic island mergers, lead to the formation of strong compression regions (X. Li et al. 2018b; J. Seo et al. 2024). These compression regions have $\alpha \approx 100 - 300\tau_A^{-1}$. For a detailed discussion of particle acceleration in the magnetic reconnection region using the MHD-SDE method, we refer interested readers to J. Seo et al. (2024). In panel (a), around y 19 Mm, a fast-mode termination shock is clearly visible in the region with $\alpha \approx 600\tau_A^{-1}$. The higher acceleration rate, , observed in this region, compared with that in the flare current sheet, can be explained by the stronger plasma compression. When large plasmoids (located between $22 \lesssim y \lesssim 27$ Mm in panel (a) of Figure 2) collide with the above-the-looptop region, the acceleration rate at the termination shock is enhanced, as shown in panel (b) around y 20 Mm, which can be attributed to stronger plasma compression. Due to this strong compression, the particle acceleration rate at the termination shock is slightly enhanced to $\alpha \approx 700\tau_A^{-1}$. However, within a few seconds after the initial contact, the collision disrupts the horizontal termination shock structure (panel (c)), consistent with the behavior reported by X. Kong et al. (2020). The shock is then restored after the plasmoid merges (panel (d)). This phenomenon shows consistency with features observed in X-ray and microwave emissions (B. Chen et al. 2015).

In this case, the feedback from nonthermal electrons suppresses the compressibility of highly compressed structures, yielding a maximum value of that is about 60% lower than in the case without feedback at a similar stage of flare evolution.

3.3. Global Distributions of Nonthermal Electrons and Their Feedback

For the first time, our simulation provides a realistic estimate of the energy carried by nonthermal electrons by including their feedback. The nonthermal electrons are primarily injected around the primary reconnection X-point, y 21 Mm in Figures 3(a) and (b). Interestingly, this region is characterized by a lack of high-energy electrons because the bidirectional exhaust from the X-point produces flow divergence, and thus compression-driven acceleration does not occur there. Once nonthermal electrons are injected, they are accelerated into high energies due to flow compression in the current sheet region and advected by the reconnection outflows. The nonthermal electrons in the downward outflows are further accelerated by the termination shock to a few hundred keV in the above-the-looptop region ($6 \leqslant y \leqslant$ 18 Mm in Figures 3(a) and (b)). Figure 3(a) shows that, at the above-the-looptop, nonthermal electrons exceeding 20 keV contain a substantial amount of energy, $E_{\rm NT,20} = \int_{20\rm keV}^{\infty} \varepsilon f(\varepsilon) d\varepsilon \sim 10$ erg cm^{-3}. For comparison, in the case with $R_i = 1\%$, $E_{\rm NT,20}$ is on the order of unity, whereas in the case with $R_i = 20\%$, it has a similar value to the $R_i = 10\%$ case. Due to the additional acceleration at the termination shock, most of these high-energy electrons are concentrated in the above-the-looptop region, with a density 2 orders of magnitude higher than that in the current sheet. These trends are also found in the EOVSA observations (B. Chen et al. 2020b). They showed a lack of high-energy nonthermal

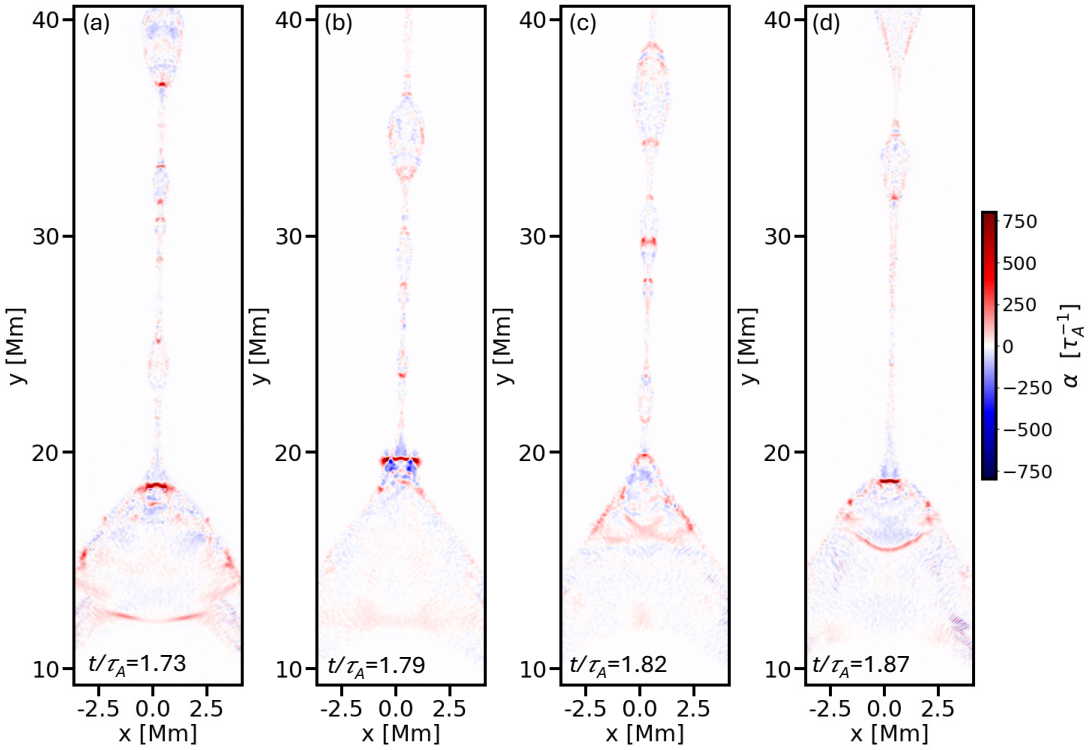

Figure 2. Snapshots of the acceleration rate at (a) $t/\tau_A = 1.73$, (b) 1.79, (c) 1.82, and (d) 1.87 for the $R_i = 10\%$ case. Only the region spanning $[-4, 4] \times [9, 41]$ Mm^2 is shown. The positive and negative values of indicate particle acceleration and deceleration, respectively.

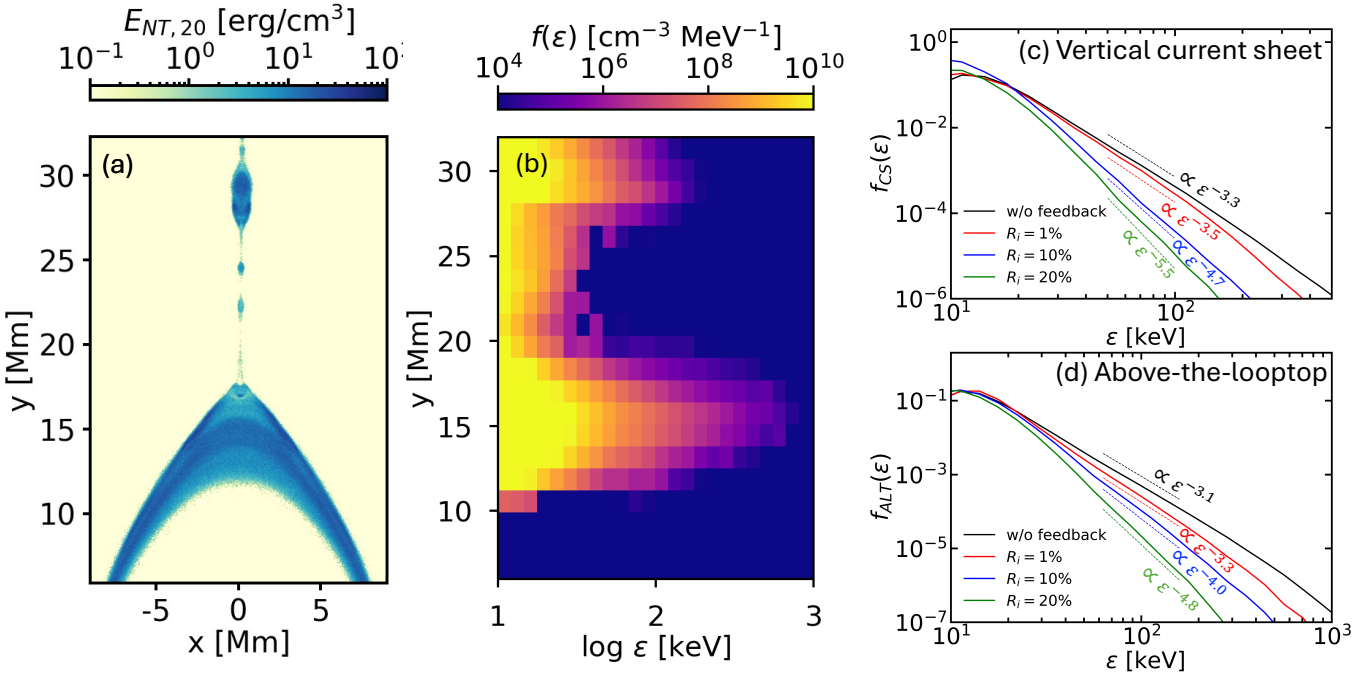

Figure 3. (a) The spatial distribution of nonthermal electron energy density with energies above 20 keV. (b) Height–energy distribution of the nonthermal electrons along the y-direction within the $-2 \leqslant x \leqslant 2$ Mm region. Panels (a) and (b) are shown at $t/\tau_A = 1.45$ and only in the domain spanning $[-10, 10] \times [6, 40]$ Mm^2. (c) Energy spectra of nonthermal electrons in the vertical current sheet ($20 \leqslant y \leqslant 40$ Mm), normalized by the total number of particles, for injection rates of 20% (green solid), 10% (blue solid), and 1% (red solid) at $t/\tau_A = 1.45$. Dashed lines indicate the power-law slopes. (d) The same as (c), but for the above-the-looptop region ($6 \leqslant y \leqslant 18$ Mm).

particles with energies above 100 keV at the primary reconnection X-point and an enrichment in the above-the-looptop region.

To illustrate the role of feedback, we compare the energy spectrum in different runs and show the results in Figures 3(c) and (d). In all these runs, the nonthermal electrons develop power-law energy spectra, and the spectral indices are within the range often observed (S. Krucker et al. 2010; M. Oka et al. 2013, 2015; F. Effenberger et al. 2017). For example, in the fiducial case ($R_i = 10\%$), the spectrum in the vertical current

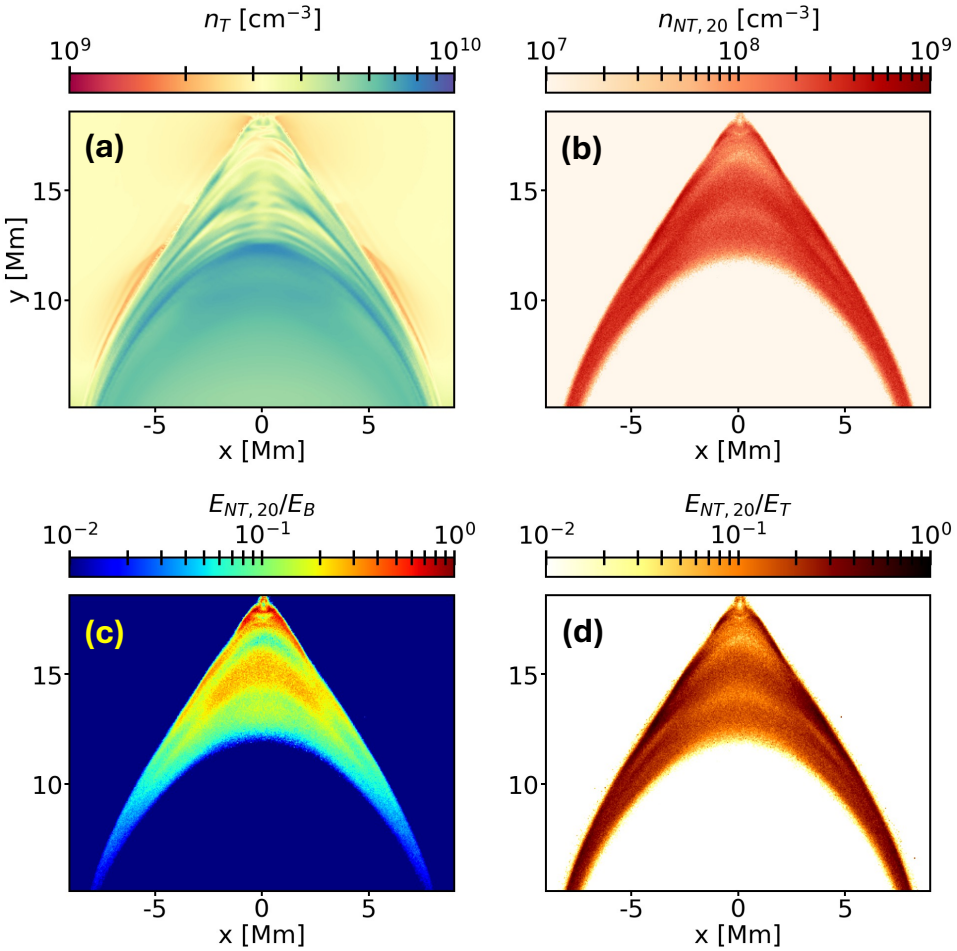

Figure 4. A snapshot showing (a) the thermal electron density n_T, (b) the nonthermal electron density $n_{\rm NT}$, (c) the ratio of nonthermal electron energy to magnetic energy $E_{\rm NT}/E_B$, and (d) the ratio between nonthermal electron energy to thermal electron energy at $t/\tau_A = 1.45$. Only the $[-10, 10] \times [6, 19]$ Mm^2 domain is shown here.

sheet $f_{\rm CS}(\varepsilon) \propto \varepsilon^{-4.7}$, and the spectrum in the above-the-looptop region $f_{\rm ATL}(\varepsilon) \propto \varepsilon^{-4.0}$, which is harder than $f_{\rm CS}$ due to the additional acceleration.

The nonthermal electron pressure provides feedback to the thermal plasma by suppressing compression structures, which in turn mediates particle energization. As a result, greater feedback from energetic particles leads to a steeper power-law energy spectrum (J. Seo et al. 2024). So, as shown in Figures 3(c) and (d), if we increase (decrease) the nonthermal fraction R_i, the spectrum will become steeper (harder). Thus, the feedback from nonthermal electrons is one of the key factors in electron acceleration and in determining the slope of the energy spectrum in solar flares. We note that, in Fermi-type acceleration mechanisms, the spectral index is primarily governed by the acceleration rate and the particle escape timescale (e.g., L. O. Drury 1983; F. Guo et al. 2014; X. Li et al. 2019b). This underscores that particle escape, in addition to acceleration, plays a fundamental role in determining the resulting energy spectrum.

3.4. Energetic Electrons Distribution in the Above-the-looptop Region

In this subsection, we focus on the features found in the above-the-looptop region, where nonthermal electrons are predominantly present. We plot (a) the thermal electron density, n_T, (b) the nonthermal electron number density, $n_{\rm NT}$, (c) the ratio of nonthermal electron energy density to magnetic energy density $E_{\rm NT,20}/E_B$, and (d) the ratio of nonthermal electron energy density to thermal plasma energy density $E_{\rm NT,20}/E_T$ in Figure 4 for the $R_i = 10\%$ case. Panel (a) reveals that the thermal electron density in the above-the-looptop region is several times lower than that in the magnetic loop region. This low-density region forms because the plasma is supplied by magnetic reconnection occurring higher up in the corona, where the background density is much lower. In this region, the thermal electron number density is $n_T \sim 3$–6×10^9 cm^{-3}. This value lies within the range observed for the thermal electron density in this region, which is 10^9–10^{10} cm^{-3} (S. Krucker et al. 2010; M. Oka et al. 2013, 2015; E. P. Kontar et al. 2023). Panel (b) shows that energetic particles are primarily concentrated in the above-the-looptop region, where $n_{\rm NT,20} = \int_{20\rm keV}^{\infty} f(\varepsilon) d\varepsilon$. In this region, the magnetic field exhibits a local minimum resembling a "magnetic bottle" (B. Chen et al. 2020b), and, as a result, the ratio $E_{\rm NT,20}/E_B$ can reach several tens of percent, as illustrated in panel (c). Moreover, the energy density of nonthermal electrons can amount to nearly half of the thermal plasma energy, $E_{\rm NT,20}/E_T \lesssim 50\%$, making it comparable in magnitude, as indicated in panel (d). We also observe higher values of $n_{\rm NT,20}/n_T$, $E_{\rm NT,20}/E_B$, and $E_{\rm NT,20}/E_T$ for larger R_i,

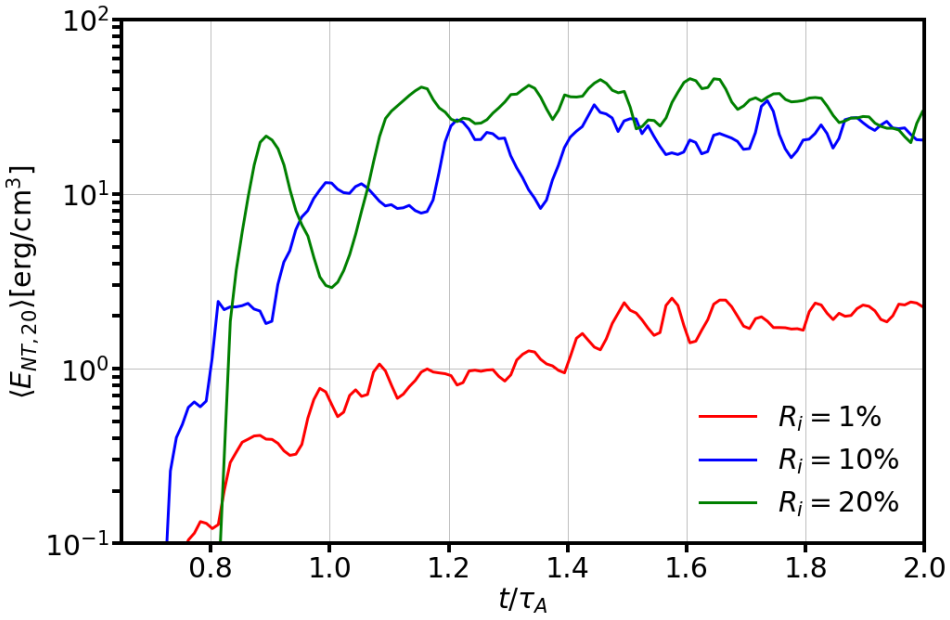

Figure 5. The time evolution of the mean energy density of nonthermal electrons with energies above 20 keV within the above-the-looptop region ($6 \leqslant y \leqslant 18$ Mm with nonthermal electron presence). The period of oscillation is $0.1\tau_A =$ a few tens of seconds, which is similar to the period of QPPs (L. A. Hayes et al. 2020).

demonstrating the model's ability to produce dominant energetic nonthermal electrons in the above-the-looptop region and further emphasizing the importance of including the feedback from energetic electrons.

The nonthermal electrons also exhibit significant temporal variability, as illustrated in Figure 5, which shows the time evolution of the nonthermal electron energy density with energy above 20 keV in the above-the-looptop region. The energy density increases up to t/τ_A 1 as the evolution of the current sheet supplies nonthermal electrons to the above-the-looptop region, and the termination shock effectively accelerates them. After t/τ_A 1, the acceleration and escape of nonthermal electrons become nearly balanced, resulting in a saturation in the mean energy density. In this quasi-steady state, particle escape plays an important role in determining the energy density in this region. During the saturation period, the mean energy density of nonthermal electrons with energies above 20 keV in the above-the-looptop region is approximately 10–30 erg cm^{-3} for the $R_i = 10\%$ and 20% cases. On top of this evolution, oscillations are observed, which correspond to the periodic impacts of large magnetic islands on the above-the-looptop region. Hence, variations in the energy density of nonthermal electrons may give rise to QPPs observed in solar flares across multiple wavelengths (S. R. Kane et al. 1983; A. R. Inglis et al. 2008; L. A. Hayes et al. 2020). The period of this variation, $0.1\tau_A$ a few tens of seconds, lies within the observed range of QPP periods. A similar phenomenon was observed during the 2010 August 18 solar flare, where plasmoid collisions with flare loops coincided with impulsive microwave bursts at 34 GHz attributed to gyrosynchrotron emission from nonthermal electrons (S. Takasao et al. 2016). In addition, A. Asai et al. (2004) reported that downward-moving plasmoids show a strong temporal correlation with impulsive nonthermal emissions.

Nonthermal electron distribution in the above-the-looptop region is also energy dependent. Figures 6(a) and (b) show the nonthermal electron density distribution for 20–40 keV and 50–150 keV, respectively, at $t/\tau_A = 1.45$. The nonthermal electrons are advected by the reconnection outflows and accumulate in the above-the-looptop region. Near the termination shock, these electrons undergo Fermi acceleration and are further energized, producing a higher-energy nonthermal population. Hence, as shown in Figures 6(a) and (b), compared to 20–40 keV electrons, 50–150 keV electrons are more prevalent in the higher region ($y > 13$ Mm) than in the lower region ($y < 13$ Mm). This trend is consistent with the results of X. Kong et al. (2019), which showed that higher-energy electrons are concentrated closer to the termination shock at higher altitudes, due to acceleration by the shock and confinement within a concave-downward magnetic trap. As a result, the electron spectrum is harder in the higher region than in the lower region, as shown in Figure 6(c). The power-law spectral index 3–4 in the higher above-the-looptop region, while 5–7 in the lower region.

In the above-the-looptop region, the power-law energy spectrum arises from first-order Fermi acceleration driven by strong plasma compression at the magnetic reconnection site and the termination shock (X. Kong et al. 2019; X. Kong et al. 2022; X. Li et al. 2022; Q. Zhang et al. 2024). The spectral slope is largely determined by the local compression ratio, while thermal conduction in hot plasma can alter the thermodynamic structure and can even modify the geometry of termination shocks (S. Takasao & K. Shibata 2016; C. Shen et al. 2018). In addition, when thermal conduction is included, the reconnection outflow Mach number depends on the plasma beta (T. Yokoyama & K. Shibata 1998, 2001; D. B. Seaton & T. G. Forbes 2009; S. Takasao & K. Shibata 2016). Notably, as shown in Figure 9 of D. B. Seaton & T. G. Forbes (2009), the effect of thermal conduction becomes significant for $\lesssim 0.01$. As discussed earlier, our current model does not incorporate several physical effects, such as thermal conduction, pressure anisotropy, and magnetic mirroring. Nevertheless, the model remains physically meaningful because it captures the essential role of feedback from nonthermal electrons in regulating particle acceleration within the flare geometry. A more

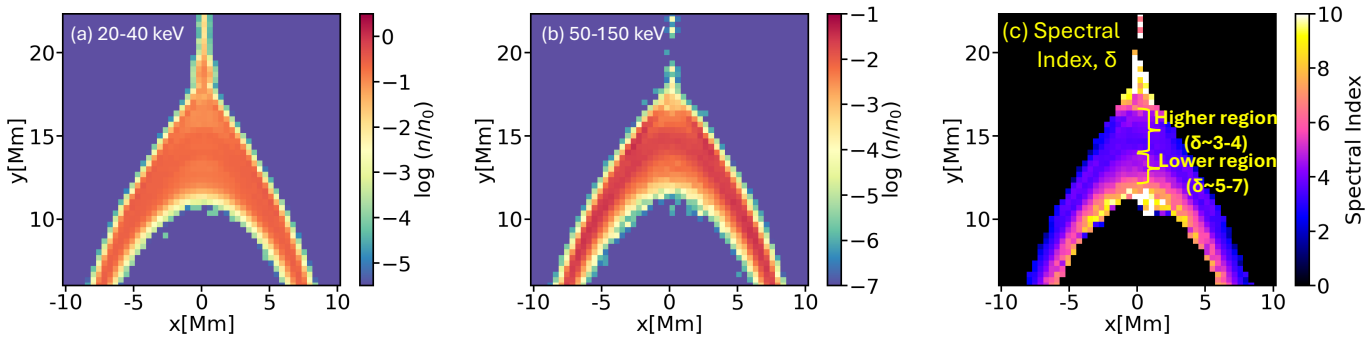

Figure 6. (a) Spatial density distribution of nonthermal electrons in the 20–40 keV range. (b) Spatial density distribution of nonthermal electrons in the 50–150 keV range. (c) The spectral index of nonthermal electrons around the flare looptop region at $t/\tau_A = 1.45$. The spectral index is measured in the range of 30–100 keV. Only the $[-10, 10] \times [6, 22]\,\mathrm{Mm}^2$ domain is shown here.

comprehensive investigation that incorporates these additional multiphysics processes is deferred to future work.

4. Summary

For the first time, we perform simulations of particle acceleration and transport in a flare eruption model, incorporating the feedback of nonthermal electrons into the MHD plasma. We find a prominent presence of high-energy nonthermal electrons in the above-the-looptop region, resulting from acceleration by the termination shock and magnetic reconnection. The main findings are summarized as follows:

1. In the fiducial model, where the injection rate is $R_i = n_{\mathrm{NT}}/n_T = 10\%$, we find a power-law energy spectrum for nonthermal electrons in the above-the-looptop region, $f_{\mathrm{ATL}}(\varepsilon) \quad \varepsilon^{-4}$, with the slope depending on the injection rate, R_i, of the nonthermal electrons.
2. As effective acceleration occurs, nonthermal electrons in the above-the-looptop region are accelerated to energies above 100 keV, which can serve as a potential explanation of observed hard X-rays and microwaves (S. Krucker et al. 2010; M. Oka et al. 2013, 2015; F. Effenberger et al. 2017; B. Chen et al. 2020b; E. P. Kontar et al. 2023).
3. At the above-the-looptop region, the energy carried by nonthermal electrons corresponds to roughly several tens of percent of the magnetic energy, $E_{\mathrm{NT},20}/E_B \quad 10\%$–$30\%$, and up to about half of the thermal energy, $E_{\mathrm{NT},20}/E_T \lesssim 50\%$, underscoring the importance of including feedback from nonthermal electrons.
4. Our model yields an energy density of nonthermal electrons with energies above 20 keV of $E_{\mathrm{NT},20} \quad 10$–$30\,\mathrm{erg\,cm^{-3}}$ in the above-the-looptop region. The impact of large magnetic islands on the above-the-looptop region occurs with a period of several tens of seconds, leading to oscillations in the energy of nonthermal electrons. These oscillations may result in the generation of QPPs (S. R. Kane et al. 1983; A. R. Inglis et al. 2008; L. A. Hayes et al. 2020).

In conclusion, our study on the acceleration of nonthermal electrons in a flare model including the above-the-looptop region shows that these electrons have a power-law energy spectrum, which is a potential explanation for coronal emissions during solar flares, even when their feedback is taken into account.

Acknowledgments

We acknowledge support from Los Alamos National Laboratory through the LDRD program, DOE OFES, and NASA programs through grants NNH17AE68I, 80HQTR20T0073, and 80HQTR21T0005, 80HQTR21T0117, NNH230B17A, and NNH240B72A. J.S. acknowledges support from the Los Alamos National Laboratory (LANL) through its Center for Space and Earth Science (CSES). CSES is funded by LANL's Laboratory Directed Research and Development (LDRD) program under project number 20240477CR. F.G. acknowledges NSF Award No. 2334932. X.L. acknowledges support from NASA grant 80NSSC21K1313, National Science Foundation grant Nos. AST-2107745 and AGS-2334930, University of California, Berkeley, through subcontract No. 00011753, and Smithsonian Astrophysical Observatory through subcontract No. SV1-21012. B.C. acknowledges support from NSF grant AST-2108853 to the New Jersey Institute of Technology (NJIT) and NASA grant NNH240B72A (through subcontract 89233218CNA000001/C5509 from LANL to NJIT). The simulations used resources provided by the Los Alamos National Laboratory Institutional Computing Program, which is supported by the U.S. Department of Energy National Nuclear Security Administration under Contract No. 89233218CNA000001, the National Energy Research Scientific Computing Center (NERSC), a Department of Energy Office of Science User Facility using NERSC award FES-ERCAP0031616, and the Texas Advanced Computing Center (TACC).

ORCID iDs

Jeongbhin Seo https://orcid.org/0000-0002-5550-8667
Fan Guo https://orcid.org/0000-0003-4315-3755
Xiaocan Li https://orcid.org/0000-0001-5278-8029
Bin Chen https://orcid.org/0000-0002-0660-3350
Chengcai Shen https://orcid.org/0000-0002-9258-4490
Hui Li https://orcid.org/0000-0003-3556-6568

References

Arnold, H., Drake, J. F., Swisdak, M., et al. 2021, PhRvL, 126, 135101
Asai, A., Yokoyama, T., Shimojo, M., & Shibata, K. 2004, ApJL, 605, L77
Bai, X.-N., Caprioli, D., Sironi, L., & Spitkovsky, A. 2015, ApJ, 809, 55
Bhattacharjee, A., Huang, Y.-M., Yang, H., & Rogers, B. 2009, PhPl, 16, 112102
Birn, J., Borovsky, J. E., & Hesse, M. 2012, PhPl, 19, 082109
Brooks, D. H., Warren, H. P., & Landi, E. 2021, ApJL, 915, L24
Bykov, A. M., Ellison, D. C., Osipov, S. M., & Vladimirov, A. E. 2014, ApJ, 789, 137
Bykov, A. M., Osipov, S. M., Uvarov, Y. A., Ellison, D. C., & Slane, P. 2024, PhRvD, 110, 023041
Carmichael, H. 1964, NASSP, 50, 451
Chen, B., Bastian, T. S., Shen, C., et al. 2015, Sci, 350, 1238
Chen, B., Kong, X., Yu, S., et al. 2024, ApJ, 971, 85

Chen, B., Shen, C., Gary, D. E., et al. 2020b, NatAs, 4, 1140
Chen, B., Yu, S., Reeves, K. K., & Gary, D. E. 2020a, ApJL, 895, L50
Dahlin, J. T., Antiochos, S. K., DeVore, C. R., Wyper, P. F., & Qiu, J. 2025, ApJ, 993, id.31
Dahlin, J. T., Antiochos, S. K., Qiu, J., & DeVore, C. R. 2022, ApJ, 932, 94
Del Zanna, G., Samra, J., Monaghan, A., et al. 2023, ApJS, 265, 11
Drake, J. F., Arnold, H., Swisdak, M., & Dahlin, J. T. 2019, PhPl, 26, 012901
Drury, L. O. 1983, RPPh, 46, 973
Effenberger, F., Rubio da Costa, F., Oka, M., et al. 2017, ApJ, 835, 124
Fleishman, G. D., Nita, G. M., Chen, B., Yu, S., & Gary, D. E. 2022, Natur, 606, 674
Forbes, T. G., & Priest, E. R. 1995, ApJ, 446, 377
French, O., Guo, F., Zhang, Q., & Uzdensky, D. A. 2023, ApJ, 948, 19
Gary, D. E., Chen, B., Dennis, B. R., et al. 2018, ApJ, 863, 83
Giacalone, J., & Jokipii, J. R. 1999, ApJ, 520, 204
Guo, F., Li, H., Daughton, W., & Liu, Y.-H. 2014, PhRvL, 113, 155005
Guo, F., Liu, Y.-H., Zenitani, S., & Hoshino, M. 2024, SSRv, 220, 43
Hayes, L. A., Inglis, A. R., Christe, S., Dennis, B., & Gallagher, P. T. 2020, ApJ, 895, 50
Hirayama, T. 1974, SoPh, 34, 323
Huang, Y.-M., & Bhattacharjee, A. 2016, ApJ, 818, 20
Inglis, A. R., Nakariakov, V. M., & Melnikov, V. F. 2008, A&A, 487, 1147
Isenberg, P. A., & Jokipii, J. R. 1979, ApJ, 234, 746
Kane, S. R., Kai, K., Kosugi, T., et al. 1983, ApJ, 271, 376
Kong, X., Chen, B., Guo, F., et al. 2022, ApJL, 941, L22
Kong, X., Guo, F., Shen, C., et al. 2019, ApJL, 887, L37
Kong, X., Guo, F., Shen, C., et al. 2020, ApJL, 905, L16
Kontar, E. P., Emslie, A. G., Motorina, G. G., & Dennis, B. R. 2023, ApJL, 947, L13
Kopp, R. A., & Pneuman, G. W. 1976, SoPh, 50, 85
Krucker, S., Hudson, H. S., Glesener, L., et al. 2010, ApJ, 714, 1108
Li, T. C., Drake, J. F., & Swisdak, M. 2013, ApJ, 778, 144
Li, X., Guo, F., Chen, B., Shen, C., & Glesener, L. 2022, ApJ, 932, 92
Li, X., Guo, F., & Li, H. 2019a, ApJ, 879, 5
Li, X., Guo, F., Li, H., & Birn, J. 2018a, ApJ, 855, 80
Li, X., Guo, F., Li, H., & Li, S. 2018b, ApJ, 866, 4
Li, X., Guo, F., Li, H., Stanier, A., & Kilian, P. 2019b, ApJ, 884, 118
Lin, H., Penn, M. J., & Tomczyk, S. 2000, ApJL, 541, L83
Lin, J., & Forbes, T. G. 2000, JGR, 105, 2375
Loureiro, N. F., Schekochihin, A. A., & Cowley, S. C. 2007, PhPl, 14, 100703
Loureiro, N. F., & Uzdensky, D. A. 2016, PPCF, 58, 014021
Ma, H., Drake, J. F., & Swisdak, M. 2023, ApJ, 954, 21
Mondal, S., Battaglia, A. F., Chen, B., & Yu, S. 2024, ApJ, 966, 208
Oka, M., Ishikawa, S., Saint-Hilaire, P., Krucker, S., & Lin, R. P. 2013, ApJ, 764, 6
Oka, M., Krucker, S., Hudson, H. S., & Saint-Hilaire, P. 2015, ApJ, 799, 129
Parker, E. N. 1965, P&SS, 13, 9
Provornikova, E., Laming, J. M., & Lukin, V. S. 2016, ApJ, 825, 55
Ruszkowski, M., & Pfrommer, C. 2023, A&ARv, 31, 4
Seaton, D. B., & Forbes, T. G. 2009, ApJ, 701, 348
Seo, J., Guo, F., Li, X., & Li, H. 2024, ApJ, 977, 146
Shen, C., Kong, X., Guo, F., Raymond, J. C., & Chen, B. 2018, ApJ, 869, 116
Sturrock, P. A. 1966, Natur, 211, 695
Sun, X., & Bai, X.-N. 2023, MNRAS, 523, 3328
Takasao, S., Asai, A., Isobe, H., & Shibata, K. 2016, ApJ, 828, 103
Takasao, S., & Shibata, K. 2016, ApJ, 823, 150
Uzdensky, D. A., Loureiro, N. F., & Schekochihin, A. A. 2010, PhRvL, 105, 235002
Wang, B.-B., Zank, G. P., Zhao, L.-L., & Adhikari, L. 2022, ApJ, 932, 65
Warmuth, A., & Mann, G. 2020, A&A, 644, A172
Warren, H. P., & Brooks, D. H. 2009, ApJ, 700, 762
Yang, Z., Bethge, C., Tian, H., et al. 2020, Sci, 369, 694
Yokoyama, T., & Shibata, K. 1998, ApJL, 494, L113
Yokoyama, T., & Shibata, K. 2001, ApJ, 549, 1160
Young, P. R., Watanabe, T., Hara, H., & Mariska, J. T. 2009, A&A, 495, 587
Zhang, Q., Guo, F., Daughton, W., Li, H., & Li, X. 2021, PhRvL, 127, 185101
Zhang, Q., Guo, F., Daughton, W., Li, X., & Li, H. 2024, ApJ, 974, 47